Nano Research

Open Access

Research Article

Improved oxygen kinetics on both cathode and anode of $SmBaFe_2O_{5+\delta}$-based solid oxide fuel cells through Ca^{2+} doping

Yumei Ma[1,§], Na Lv[1,§], Hao Song[2,§], Zhiwei Wang[1], Chao Ren[1], Yanyan Xu[1], Lina Su[1] ✉, and Ling Huang[1,2] ✉

[1] *State Key Laboratory of Chemistry and Utilization of Carbon-Based Energy Resources, College of Chemistry, Xinjiang University, Urumqi 830046, China*
[2] *Institute of Advanced Materials (IAM), Nanjing Tech University, Nanjing 211816, China*
§ *Yumei Ma, Na Lv, and Hao Song contributed equally to this work.*

Cite this article: *Nano Research*, **2026**, *19*, 94908918. https://doi.org/10.26599/NR.2026.94908918

ABSTRACT: Electrode materials with robust stability and outstanding catalytic activity are crucial for practical implementation of solid oxide fuel cells (SOFCs). To avoid the inherent thermal expansion from Co-based analogous, we report a double perovskite, $SmBaFe_2O_{5+\delta}$ (SBF), where purposely doping of larger Ca^{2+} (1.34 Å) in the Sm^{3+} (1.24 Å) site, widens the Fe–O–Fe angle from 162° to 168°, shortens the Fe–O(2) bond from 1.9898 to 1.9675 Å. Consequently, both the oxygen kinetics, i.e., oxygen vacancy (V_O) concentration, and electron conductivity are significantly improved, which finally leads to a high peak power density (PPD) of 2.14 and 1.18 W·cm^{-2} at 800 °C among Fe-based perovskites, for single cell using $Sm_{0.9}Ca_{0.1}BaFe_2O_{5+\delta}$ (SCBF) as cathode and symmetrical-SOFC (Sym-SOFC) using SCBF as both cathode and anode, respectively. This work provides a fresh angle for the design of Co-free, high-performance, and cost-effective electrode materials for SOFCs.

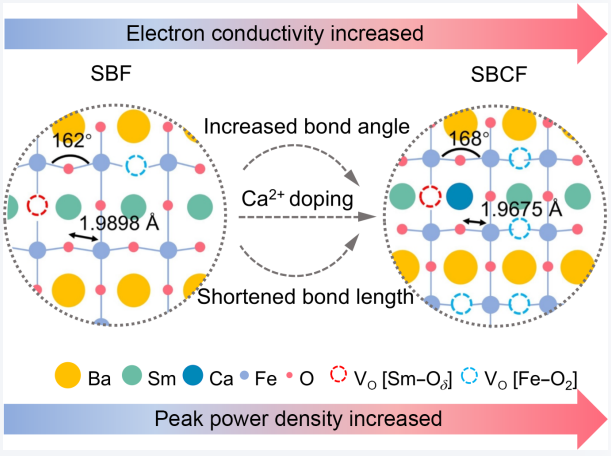

KEYWORDS: solid oxide fuel cell, $SmBaFe_2O_{5+\delta}$, Ca^{2+} doping, oxygen kinetics, cathode/anode

1 Introduction

The fast-growing reliance on artificial intelligence-derived applications, electric vehicles, and portable electronic devices, together with the decreased reserve of crude oil and natural gas, has brought significant pressure on electricity production. Exploration for alternative electricity sources, including solar energy, wind energy, and hydro energy, has thus become an indispensable supplement. Due to the high conversion efficiency, wide fuel flexibility, and environmentally friendly emissions, solid oxide fuel cells (SOFCs) hold great potential in chemical-to-electricity generation, particularly in vehicles, power plants, and stringent circumstances [1–3]. However, the sluggish oxygen reduction reaction (ORR) kinetics that occur on the cathode remain a major source of polarization loss in SOFCs, which severely deteriorates the output performance [4–7].

As a recently prevalent cathode material with mixed ion and electron conductivities (MIECs), swift oxygen ion transport, and efficient surface oxygen exchange, Co-based perovskites have been successively developed. Unfortunately, the inherent high thermal expansion coefficient (TEC) generates increased interfacial tension at high temperature in SOFC [8–11], causing electrode delamination and thus remaining as a major bottleneck to practical applications.

Even though the MIECs is about one order of magnitude lower than those of Co-based analogous, Fe-based layered double perovskites, $LnBaFe_2O_{5+\delta}$ (Ln = La, Pr, Sm, Nd, Gd, and Y), stacked at the sequence of [BaO]–[FeO_2]–[LnO_δ]–[FeO_2]–[BaO] along the *c*-axis has emerged as a promising alternative, due to their low cost, easy synthesis, excellent high-temperature stability, and negligible TEC [12–15]. The alternating arrangement of Ln^{3+} and Ba^{2+} planar structures weakens the oxygen binding strength, thereby facilitating the formation of oxygen vacancy (V_O) within [LnO_δ] layers. Meanwhile, the electron conduction in $LnBaFe_2O_{5+\delta}$ is mainly caused by the Fe^{4+}/Fe^{3+} polaron couples, where the holes ($h^{\cdot}$ = Fe_{Fe})

Received: February 5, 2026; **Revised:** June 6, 2026
Accepted: June 8, 2026

✉Address correspondence to Lina Su, sulina@xju.edu.cn; Ling Huang, huangling@zju.edu.cn

hop along the Fe–O–Fe bond in the lattice [16, 17]. Therefore, the 180° Fe–O–Fe bond angle is ideal for electron transport [18, 19]. However, the radius disparity between Ln^{3+} and Ba^{2+} deviates the Fe–O–Fe bond away from the ideal angle, which is unfavorable to electron conductivity and electrochemical activity of $LnBaFe_2O_{5+\delta}$ [20–25].

Herein we report, as illustrated in Fig. 1, that the radius difference between Sm^{3+} (r = 1.24 Å) and Ba^{2+} (r = 1.61 Å) can be effectively mitigated by purposely substituting the Sm^{3+} site by larger Ca^{2+} (r = 1.34 Å) in $SmBaFe_2O_{5+\delta}$ (SBF) to form $Sm_{0.9}Ca_{0.1}BaFe_2O_{5+\delta}$ (SCBF), so that the Fe–O–Fe bond angle can be widened from 162° to 168° and the Fe–O(2) bond length shortened from 1.9898 to 1.9675 Å.

Meanwhile, substitution of Sm^{3+} by lower-valent Ca^{2+} also increases the oxidation state of Fe ions due to charge compensation. These synergistic changes in bond angle, bond length, and Fe valence state brings a 91% electrical conductivity improvement (from 5.98 to 11.42 S·cm^{-1}), 27.9% polarization resistance (R_p) reduction (from 0.043 to 0.031 Ω·cm^2), and 21% V_O concentration increase (δ, which denotes the deviation from the ideal oxygen stoichiometry, decreases from 0.61 to 0.48) in SCBF at 800 °C, which finally leads to a rather high peak power density (PPD) of 2.14 and 1.18 W·cm^{-2} for the single cell using SCBF as cathode and symmetrical-SOFC (Sym-SOFC) using SCBF as both cathode and anode, respectively, among Co-free double perovskites analogous.

2 Results and discussion

The tetragonal (*P4/mmm*) double perovskite structure of SBF (Fig. S1 and Table S1 in the Electronic Supplementary Material (ESM)) remains, though substitution of Sm^{3+} by larger Ca^{2+} reduces the radius difference between the Sm^{3+} and Ba^{2+} sites and causes a unit cell volume shrinkage (from 121.602 to 121.519 Å^3). The identical high temperature (30–900 °C) X-ray diffraction (XRD) patterns indicate no formation of new phases (Fig. S2 in the ESM), and thus excellent crystal structure stability over the entire operating temperature range. Shift of the overall diffraction peaks towards lower angles with increasing temperature is primarily due to thermal expansion of the $Sm_{0.9}Ca_{0.1}BaFe_2O_{5+\delta}$ (SBCF) lattice and the loss of lattice oxygen, which makes Fe^{4+} (r = 0.57 Å) reduced to larger-sized Fe^{3+} (r = 0.65 Å) and Fe^{2+} (r = 0.78 Å), and chemically expands the unit cell [26]. Furthermore, the Ca^{2+} doping has a negligible effect on the TEC of SBF (Fig. S3 in the ESM). In parallel, no phase change after calcination of SBF and SCBF in both the air and H_2 atmospheres (Fig. S4 in the ESM) suggests excellent chemical stability when working under cathodic and anodic environments. Moreover, shift of all the XRD peaks of H_2-reduced samples to smaller angles implies the reduction of Fe^{4+} to Fe^{3+}, which expands the unit cell and generates additional V_O.

Highly consistent with the X-ray photoelectron spectroscopy (XPS) results of Fe 2p (Fig. 2(a) and Fig. S5 and Table S2 in the ESM), shift of the Fe K-edge absorption peak to higher energy in SCBF relative to SBF (Fig. 2(b)) indicates a charge compensation triggered by the doping of lower-valent Ca^{2+} into Sm^{3+} position. This increases both the average oxidation state of Fe ions (Fig. S6 in the ESM) and hole concentration [27], which contributes to improved electron conductivity in SCBF. Meanwhile, the lattice shrinkage caused by Ca^{2+} doping (Table S1 in the ESM and Fig. 2(c)) widens the Fe–O–Fe bond angle towards the ideal value (from 162° to 168°), shortens the Fe–O(2) bond length (from 1.9898 to 1.9675 Å), and finally improves electron conductivity of SCBF.

Density functional theory (DFT) calculation further indicates that the reaction steps in the ORR process of SBF and SCBF cathode (Fig. 2(d)) are both composed of the adsorption of free O_2 molecules at (i) the catalyst active site, (ii) activation of $O_{2,ads}$ ($O_{2,ads}$ denotes the oxygen molecules adsorbed on the surface of the material), and (iii) formation of $2O_{ads}$ (O_{ads} denotes the adsorbed oxygen atoms) by breaking the O=O double bond. The results show that the free energy of each sub-reaction of SCBF (−3.481 and −4.117 eV) is lower than that of SBF (−3.335 and −3.911 eV), indicating that the ORR reaction of SCBF is thermodynamically more favorable. It should be noted that the above DFT calculations focus on the thermodynamic favorability of ORR steps (i.e., free energy changes), rather than the kinetic activation energy barriers (e.g., for O_2 adsorption and O=O bond dissociation). While the lower free energy of SCBF suggests thermodynamically enhanced ORR, full kinetic validation would require calculation of activation barriers, where as future work, first-principles calculations are needed to compute these barriers and further validate the proposed structure–performance correlations. The partial density of states (PDOS) results suggest that the −3.742 eV d-band center of SCBF is closer to the Fermi level than the −4.096 eV of SBF (Fig. S7 in the ESM), which is more propitious to O_2 adsorption and electron transfer [28]. Meanwhile, increase in the O 2p band center (E_p)

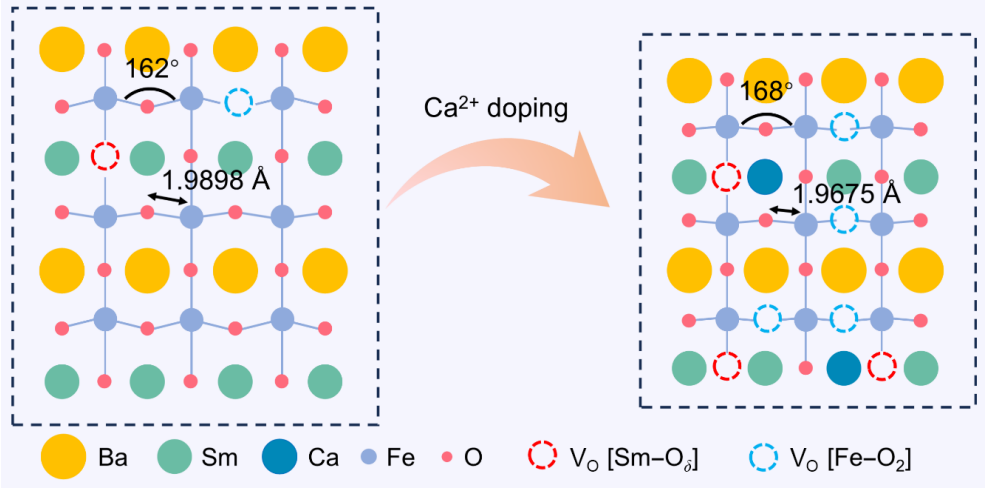

Figure 1 Schematic diagram illustrating the crystal structure evolution from SBF to SCBF caused by Ca^{2+} doping.

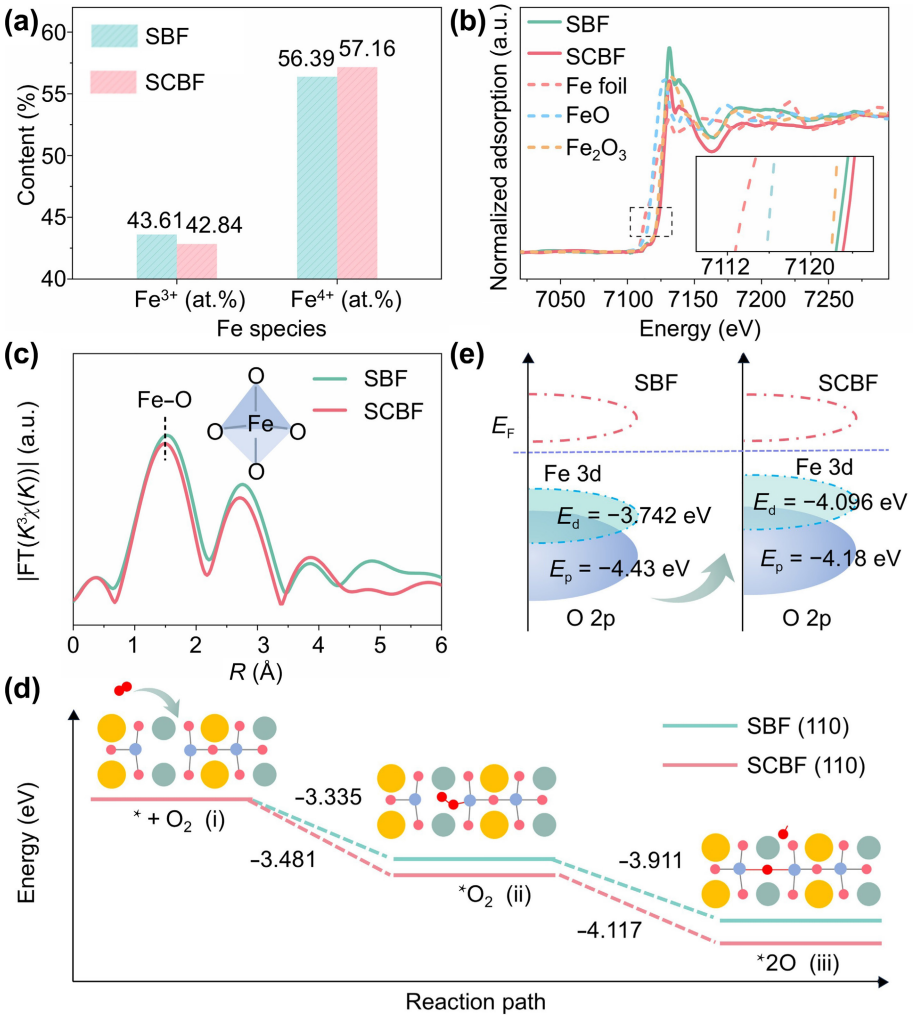

Figure 2 (a) The X-ray absorption near-edge structure (XANES) spectra of Fe K-edge in SBF and SCBF. (b) Comparison of standard samples to show the valence state change of Fe. (c) Fourier transform of the extended X-ray absorption fine structure (EXAFS) spectra. (d) Schematic diagram of the corresponding ORR path. (e) Shift of the Fe d-band center and O p-band center after Ca^{2+} doping.

from −4.43 eV in SBF to −4.18 eV in SCBF after Ca^{2+} doping (Fig. 2(e)) indicates an improved ORR activity [29], i.e., SCBF is thermodynamically more favorable to O_2 adsorption and dissociation than SBF [28, 30–34].

The V_O regulation, including density, formation energy, and migration barriers, is one of the key parameters for improving the output performance of cathode. In SBF and SCBF, V_O mainly comes from [Sm–O_δ] and [Fe–O_2] layer. The lower V_O formation energy (E_{vf}) seen in DFT calculation results (Fig. 3(a)) suggests higher V_O concentration in SCBF, which agrees well with the stronger electron spin resonance (ESR) signal (F center, g = 2.003) [35] than that of SBF (Fig. 3(b)). This is also reflected by the formation of more V_O for O_2 adsorption/dissociation in SCBF (41.06%) than that in SBF (39.50%), as observed from the fitted O 1s XPS spectra (Fig. 3(c) and Table S3 in the ESM).

Thermogravimetry analyses (TGA) below 300 °C show larger weight loss of desorbed water and gases in SCBF (0.447%) than that in SBF (0.185%), suggesting improved surface adsorption capacity after Ca^{2+} doping (Fig. 3(d)). The weight loss above 300 °C can be attributed to the thermal reduction of Fe^{4+} to Fe^{3+} and the concomitant release of lattice oxygen, which leads to the formation of more V_O in SCBF. The lowered value of 5 + δ in SCBF (5.48) compared with that in SBF (5.61) at 800 °C, as derived from high-temperature TGA (Fig. S8 in the ESM), further supports the higher V_O density in SCBF.

Electrical conductivity relaxation (ECR) is employed to characterize oxygen surface exchange coefficient (K_{ex}) and oxygen bulk diffusion coefficient (D_{chem}) in SBF and SCBF. The shorter ECR (~ 900 s) equilibrium time in SCBF than that in SBF (~ 1500 s) at 750 °C when the atmosphere is suddenly switched from air to oxygen, shows improved oxygen transport kinetics in SCBF (Fig. 3(e) and Fig. S9 in the ESM). Moreover, the higher K_{ex} and D_{chem} together with lower activation energy in SCBF over the entire temperature range (Fig. 3(f) and Fig. S10 and Table S4 in the ESM), demonstrate a faster oxygen surface exchange and bulk diffusion capability in SCBF than those in SBF.

SCBF exhibits an R_p of 0.031 Ω·cm², which is lower than the previously reported best value of 0.043 Ω·cm² for $BaCO_3$@$SmBaFe_2O_5$ (Fig. 4(a) and Fig. S11 and Table S5 in the ESM), suggesting that the highest ORR catalytic activity is obtained in SCBF. Figure 4(b) depicts the distribution of relaxation times (DRT) results extracted from the electrochemical impedance spectroscopy (EIS) of SBF and SCBF at 750 °C following the function of $F(\tau) = \tau G(\tau)\ln 10$, where $F(\tau)$ means the distribution

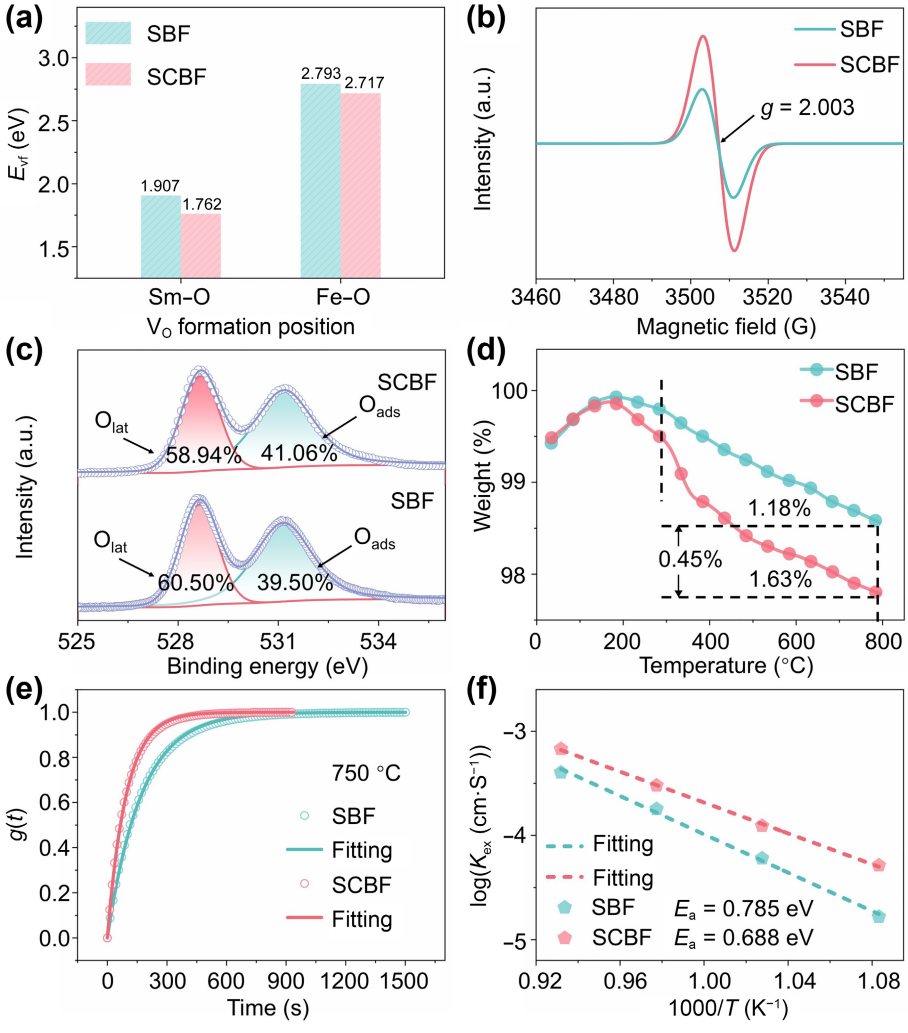

Figure 3 Physicochemical properties of SBF and SCBF: (a) The E_{vf} derived from the DFT calculation results in the ESM. (b) ESR signals of V_O. (c) XPS spectra and the fitting results of O 1s. (d) Comparison of the TGA curves. (e) Conductivity relaxation profiles measured at 750 °C. (f) The Arrhenius plots of K_{ex}.

function of the logarithm for relaxation times τ in the EIS data, τ is defined as a function of frequency, and $G(\tau)$ is the DRT of impedance [36, 37]. Compared with SBF, the peak area of both high (P_H') and middle frequency (P_M') is significantly reduced. The very slow growth of R_p in SCBF symmetrical cell during the 250 h open circuit test suggests better electrochemical stability than that of SBF (Fig. 4(c)). The EIS of SCBF symmetrical cell is collected under varying oxygen partial pressures ($P(O_2)$) to elucidate the ORR mechanism, where decrease in R_p measured at 750 °C indicates accelerated ORR at higher $P(O_2)$ (Fig. S12(a) in the ESM).

Each peak in DRT represents a sub-step in the ORR process (Fig. S12(b) in the ESM), and the integrated area under the peak is the R_p of the corresponding sub-step [38, 39]. The peak area of P_H' does not change with $P(O_2)$, while the positions of P_M' and low frequency (P_L') not only shift to higher frequency direction, the peak area also gradually decreases (Fig. 4(d)), implying that high $P(O_2)$ promotes the P_M' and P_L' reaction steps.

The relationship between $P(O_2)$ and R_p can be expressed as

$$R_p = k(P(O_2))^{-n} \quad (1)$$

Each primitive reaction has a corresponding n value (the reaction order related to the electrochemical reaction steps), through which the rate-limiting step of a sub-step can be determined [40]. As shown in Fig. 4(d), the high frequency polarization resistance (R_H) with n = 0.036 is not related to $P(O_2)$, but dependent on transmission process of oxygen ions from the electrode–electrolyte interface. The mediate frequency polarization resistance (R_M) with n = 0.473 is related to the dissociation of $O_{2,ads}$ to $2O_{ads}$, while the low frequency polarization resistance (R_L) with n = 1.663 is related to the diffusion and adsorption of oxygen [28, 32].

In the Ni-YSZ anode-supported single cell, where $(ZrO_2)_{0.92}(Y_2O_3)_{0.08}$ (YSZ) is employed as electrolyte, and $Gd_{0.1}Ce_{0.9}O_{2-\delta}$ (GDC) as barrier layer (Fig. S13 in the ESM), a PPD improvement of 76.86%, 86.59%, 97.87%, and 91.67% is obtained using SCBF as cathodes compared with those of SBF at operating temperatures of 800, 750, 700, and 650 °C, respectively (Fig. 4(e) and Figs. S14(a) and S14(b) in the ESM). It is worth emphasizing that the 2.14 W·cm^{-2} remains very high among the reported analogous (Tables S6–S8 in the ESM). The comparable Ohmic resistance (R_O) of the two cells at the same temperature rules out the contribution of differences in electrolyte thickness to the performance variations (Figs. S14(c), S14(d), and S15 in the ESM). Furthermore, the constant voltage of 0.7 V with a negligible decay rate of ~ 2.2 × 10^{-4} A·cm^2·h^{-1} for nearly 200 h operation at 750 °C proves the excellent long-term stability and highly reliable output

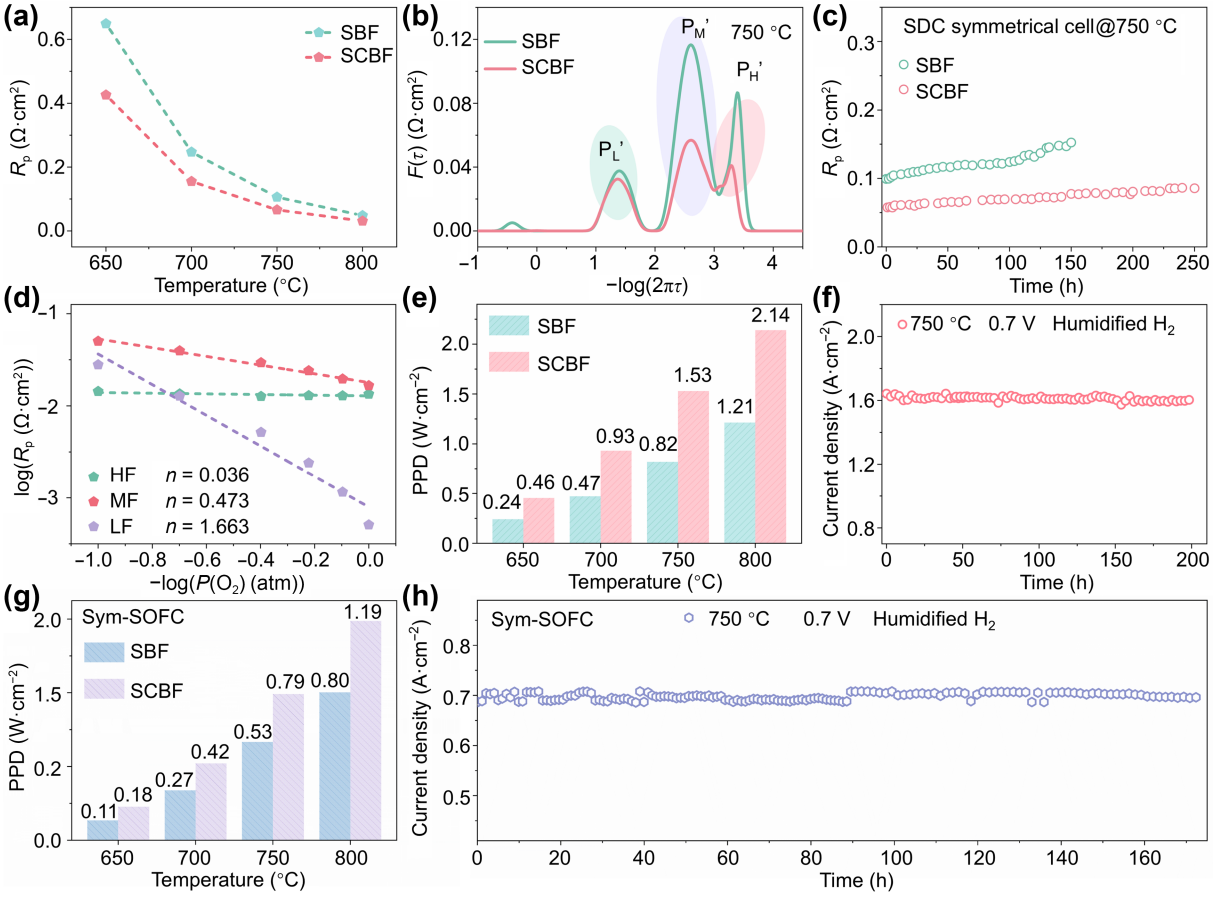

Figure 4 Electrocatalytic activity of SBF and SCBF: (a) The R_p. (b) EIS measured at 750 °C corresponding to DRT analysis in air. (c) Time-dependent R_p values at 750 °C. (d) DRT analysis of the EIS data in SCBF was conducted at varying $P(O_2)$ at 750 °C. *n* values are the corresponding fitting results. The anode-supported single cell: (e) PPD comparison of SBF and SCBF at 800–650 °C. (f) Stability of SCBF at a potential of 0.7 V. The Sym-SOFC: (g) PPD comparison of SBF and SCBF at 800–650 °C. (h) Stability of SCBF at a potential of 0.7 V.

performance using SCBF as cathode (Fig. 4(f)). Meanwhile, no cracks or holes are seen in the intermediate 12 μm thick electrolyte (Fig. S15 in the ESM), indicating that the cell fabrication process is of high quality and the density of the electrolyte is sufficient to ensure the airtightness and a high open-circuit voltage (OCV).

The anode reaction of the oxygen ion-conducting-type SOFC is strongly associated with the concentration of H_2 and H_2O vapor. The overall anode reaction (hydrogen oxidation reaction (HOR)) can be described as

$$H_2 + O_O^{\times} \rightarrow H_2O + 5V_O^{\cdot\cdot} + 2e' \quad (2)$$

where $O_O^{\times}$ denotes an oxygen ion occupying a normal oxygen lattice site, with zero effective charge relative to the perfect crystal; $V_O^{\cdot\cdot}$ denotes an oxygen vacancy with a double-positive effective charge; and e' denotes an electron with a single negative effective charge.

Therefore, the R_p of the anode is related to the partial pressure of H_2 ($P(H_2)$) and H_2O vapor ($P(H_2O)$), which can be expressed by Eq. (3)

$$R_P = k_a(P(H_2))^{(-m)}(P(H_2O))^q \quad (3)$$

The k_a is a constant. *m* and *q* are the reaction partial orders [41–43], which reflect the influence of the $P(H_2)$ and $P(H_2O)$, respectively [42, 43]. As illustrated in Fig. S16 in the ESM, the HOR can be separated into five elemental steps. If the $P(H_2O)$ is fixed, then the specific reaction steps can be distinguished according to the dependence of the R_p on the $P(H_2)$ in each step (*m* exponent). For HOR, gaseous H_2 is first adsorbed on the anode surface (H1 process), followed by dissociation of adsorbed H_2 (H2). H3 represents oxygen ion transport across the oxide interface (electrolyte and/or anode). H4 denotes the charge transfer process, where H_{ad} (the adsorbed hydrogen atom) combines with lattice oxygen to form adsorbed H_2O, V_O, and electrons. H5 is the desorption of adsorbed H_2O molecules.

Figures S17(a) and S17(b) in the ESM show the response of SBF and SCBF anodes to H_2 at 800–650 °C. Ca^{2+} doping significantly reduces the R_p of SBF under H_2 atmosphere (Fig. S17(c) in the ESM). Figure S17(d) in the ESM illustrates the response of the SCBF to varying $P(H_2)$ at 750 °C. To resolve the contribution of individual reaction steps to total R_p, DRT analysis was applied to the EIS (Fig. S17(e) in the ESM). The peak intensity decreases with increasing $P(H_2)$, and the characteristic frequency of each peak rises monotonically, indicating enhanced electrode kinetics. The P_L' contributes most to the substantial R_p reduction as $P(H_2)$ increases, identifying it as the main rate-limiting step of the anode process.

The integrated peak area corresponds to R_p of each sub-reaction. From the dependence of each sub-reaction's R_p on $P(H_2)$, the exponent *m* for each elementary step in Fig. S17(f) in the ESM can be derived, allowing assignment of the corresponding process for each peak. P_L' is assigned to H_2O vapor desorption. For the P_H', the derived $m = 0$ corresponds to oxygen ion transport at the

electrolyte/anode interface. The P_M' gives m = 0.5, indicating $H_{2,ad}$ (hydrogen molecules adsorbed on the surface of the material) dissociation. These results identify H_2O vapor desorption as the rate-limiting step for the SCBF anode.

The OCV of the Sym-SOFC with identical cathode and anode materials is close to 1.01 V at different temperatures, as shown in the current density–power density–voltage curves and EIS (Figs. S18 and S19 in the ESM). The PPD is improved 48.2%, 48.8%, 53.9%, and 68.5% in SCBF-based Sym-SOFC compared with those of SBF at 800, 750, 700, and 650 °C, respectively (Fig. 4(g)). When compared with other double perovskites, such as $Sr_2Fe_{1.5}Mo_{0.5}O_{6-\delta}$ (SFM)-based materials, SCBF exhibits not only a lower R_p but also faster oxygen kinetics (Table S9 in the ESM). The good bonding with the electrolyte without any delamination during the 175 h test at 750 °C and 0.7 V (Fig. 4(h)), together with the stable current density of 0.7 A·cm^{-2}, indicates reliable performance of the Sym-SOFC, making it a very promising candidate for symmetrical electrode as well. Figures S20 and S21 in the ESM show the scanning electron microscopy (SEM) and XRD results of the anode side of the symmetric cell after testing, which indicate no significant morphological degradation or secondary phase formation on the anode surface. The XRD pattern remains consistent with the pristine phase, confirming the excellent chemical and structural stability of the material under the test conditions. After passing the stability test, the cross-section of the symmetric single cell and the microstructure of the electrodes show that the single cell maintains an intact microstructure in both air and humidified H_2 atmospheres. The electrode–electrolyte interface remains tightly bonded without any delamination or cracking, confirming good interfacial compatibility and matched thermal expansion behavior between the two components.

To verify the mechanical and electrochemical stability of the Sym-SOFC during thermal cycling, we simultaneously monitored the electrochemical performance throughout the thermal cycling tests. The results show that after 20 thermal cycles, the PPD decreases from 1.19 to 1.18 W·cm^{-2} (Fig. S22(a) in the ESM), while the R_p increases slightly from an initial value of 0.151 to 0.158 Ω·cm^2 (Fig. S22(b) in the ESM). These changes are within an acceptable range. Furthermore, the post-cycling SEM images (Figs. S22(c) and S22(d) in the ESM) reveal no observable delamination or cracks, further confirming the structural integrity and stability of the cell under thermal cycling conditions.

3 Conclusions

A novel cathode and anode material of SCBF with excellent physical and chemical stability in both oxidizing and reducing atmospheres, as well as significantly improved oxygen kinetics, has been successfully synthesized through doping of Ca^{2+} into the Sm^{3+} position, which brings nearly doubled conductivity and 40% reduced R_p compared with those of SBF at 800 °C in an air atmosphere. The PPD of 2.14 and 1.18 W·cm^{-2} of the SCBF anode-supported single cell and SCBF-based Sym-SOFC at 800 °C, respectively, is quite a high value among currently reported Co-free Fe-based double perovskites, making SCBF a highly promising electrode material for SOFC. We also anticipate that the strategy showcased herein shall be further extendable to the design of other functional materials.

Electronic Supplementary Material: Supplementary material (synthesis methods, cell preparation processes, characterization equipment, DFT calculations, XRD patterns, SEM images, TEM measurement, TEC curves, EIS analysis, and XPS fitting results) is available in the online version of this article at https://doi.org/10.26599/NR.2026.94908918.

Data availability

All data needed to support the conclusions in the paper are presented in the manuscript and the Electronic Supplementary Material. Additional data related to this paper may be requested from the corresponding author upon request.

Acknowledgements

This work was supported by the Xinjiang Autonomous Region Key Research Project (No. 2022D01D31) and the Key Program of the National Natural Science Foundation of China (No. 22435003).

Declaration of competing interest

All the contributing authors report no conflict of interests in this work.

Author contribution statement

Y. M. M.: Methodology, validation, data curation, writing – original draft. N. L.: Data curation, validation, writing and review & editing. H. S.: Data curation, project administration, validation, writing – review & editing. Z. W. W.: Validation, data curation. C. R.: Validation, data curation. Y. Y. X.: Validation, data curation. L. N. S.: Conceptualization, project administration, funding acquisition, writing and editing manuscript. L. H.: Conceptualization, project administration, funding acquisition, writing and editing manuscript. All authors have read and approved the final manuscript.

Use of AI statement

None.

References

[1] Wachsman, E. D.; Lee, K. T. Lowering the temperature of solid oxide fuel cells. *Science* **2011**, *334*, 935–939.

[2] Xia, C.; Mi, Y. Q.; Wang, B. Y.; Lin, B.; Chen, G.; Zhu, B. Shaping triple-conducting semiconductor $BaCo_{0.4}Fe_{0.4}Zr_{0.1}Y_{0.1}O_{3-\delta}$ into an electrolyte for low-temperature solid oxide fuel cells. *Nat. Commun.* **2019**, *10*, 1707.

[3] Zhou, Y.; Guan, X. F.; Zhou, H.; Ramadoss, K.; Adam, S.; Liu, H. J.; Lee, S.; Shi, J.; Tsuchiya, M.; Fong, D. D. et al. Strongly correlated perovskite fuel cells. *Nature* **2016**, *534*, 231–234.

[4] Kim, J.; Sengodan, S.; Kwon, G.; Ding, D.; Shin, J.; Liu, M. L.; Kim, G. Triple-conducting layered perovskites as cathode materials for proton-conducting solid oxide fuel cells. *ChemSusChem* **2014**, *7*, 2811–2815.

[5] Shin, S. S.; Kim, J. H.; Jeong, H.; Park, M. Y.; Yoon, K. J.; Son, J. W.; Choi, M.; Kim, H. Vapor-mediated infiltration of nanocatalysts for low-temperature solid oxide fuel cells using electrosprayed dendrites. *Nano Lett.* **2021**, *21*, 10186–10192.

[6] Mahato, N.; Banerjee, A.; Gupta, A.; Omar, S.; Balani, K. Progress in material selection for solid oxide fuel cell technology: A review. *Prog. Mater. Sci.* **2015**, *72*, 141–337.

[7] Zamudio-García, J.; Caizán-Juanarena, L.; Porras-Vázquez, J. M.; Losilla, E. R.; Marrero-López, D. A review on recent advances and

trends in symmetrical electrodes for solid oxide cells. *J. Power Sources* **2022**, *520*, 230852.

[8] Gao, L.; Li, Q.; Sun, L. P.; Zhang, X. F.; Huo, L. H.; Zhao, H.; Grenier, J. C. A novel family of Nb-doped $Bi_{0.5}Sr_{0.5}FeO_{3-\delta}$ perovskite as cathode material for intermediate-temperature solid oxide fuel cells. *J. Power Sources* **2017**, *371*, 86–95.

[9] Tian, Y. F.; Wang, W. J.; Liu, Y.; Zhang, L. L.; Jia, L. C.; Yang, J.; Chi, B.; Pu, J.; Li, J. Cobalt-free perovskite oxide $La_{0.6}Sr_{0.4}Fe_{0.8}Ni_{0.2}O_{3-\delta}$ as active and robust oxygen electrode for reversible solid oxide cells. *ACS Appl. Energy Mater.* **2019**, *2*, 3297–3305.

[10] Wan, Y. H.; Xing, Y. L.; Li, Y. H.; Huan, D. M.; Xia, C. R. Thermal cycling durability improved by doping fluorine to $PrBaCo_2O_{5+\delta}$ as oxygen reduction reaction electrocatalyst in intermediate-temperature solid oxide fuel cells. *J. Power Sources* **2018**, *402*, 363–372.

[11] Muñoz-Gil, D.; Pérez-Coll, D.; Urones-Garrote, E.; Amador, U.; García-Martín, S. Influence of the synthesis conditions on the crystal structure and properties of $GdBaCo_{2-x}Fe_xO_{5+\delta}$ oxides as air-electrodes for intermediate temperature solid oxide fuel cells. *J. Mater. Chem. A* **2017**, *5*, 12550–12556.

[12] Chen, T.; Pang, S. L.; Shen, X. Q.; Jiang, X. N.; Wang, W. Z. Evaluation of Ba-deficient $PrBa_{1-x}Fe_2O_{5+\delta}$ oxides as cathode materials for intermediate-temperature solid oxide fuel cells. *RSC Adv.* **2016**, *6*, 13829–13836.

[13] Lee, D.; Kim, D.; Son, S. J.; Kwon, Y. I.; Lee, Y.; Ahn, J. H.; Joo, J. H. Simultaneous A- and B-site substituted double perovskite (AA' $B_2O_{5+\delta}$) as a new high-performance and redox-stable anode material for solid oxide fuel cells. *J. Power Sources* **2019**, *434*, 226743.

[14] Lu, Y.; Zhao, H. L.; Li, K.; Du, X. F.; Ma, Y. H.; Chang, X. W.; Chen, N.; Zheng, K.; Świerczek, K. Effective calcium doping at the B-site of $BaFeO_{3-\delta}$ perovskite: Towards low-cost and high-performance oxygen permeation membranes. *J. Mater. Chem. A* **2017**, *5*, 7999–8009.

[15] Zhang, Z. B.; Zhu, Y. L.; Zhong, Y. J.; Zhou, W.; Shao, Z. P. Anion doping: A new strategy for developing high-performance perovskite-type cathode materials of solid oxide fuel cells. *Adv. Energy Mater.* **2017**, *7*, 1700242.

[16] Sengodan, S.; Choi, S.; Jun, A.; Shin, T. H.; Ju, Y. W.; Jeong, H. Y.; Shin, J.; Irvine, J. T. S.; Kim, G. Layered oxygen-deficient double perovskite as an efficient and stable anode for direct hydrocarbon solid oxide fuel cells. *Nat. Mater.* **2015**, *14*, 205–209.

[17] Dong, X. L.; Jin, W. Q.; Xu, N. P. Reduction-tolerant oxygen-permeable perovskite-type oxide $Sr_{0.7}Ba_{0.3}Fe_{0.9}Mo_{0.1}O_{3-\delta}$. *Chem. Mater.* **2010**, *22*, 3610–3618.

[18] Lü, S. Q.; Zhu, Y. Z.; Fu, X. M.; Huang, R.; Guo, Y. Q.; Zhang, W. X.; Li, H. L.; Hou, L. J.; Meng, X. W. A-site deficient Fe-based double perovskite oxides $Pr_xBaFe_2O_{5+\delta}$ as cathodes for solid oxide fuel cells. *J. Alloys Compd.* **2022**, *911*, 165002.

[19] Zhang, K.; Ge, L.; Ran, R.; Shao, Z. P.; Liu, S. M. Synthesis, characterization and evaluation of cation-ordered $LnBaCo_2O_{5+\delta}$ as materials of oxygen permeation membranes and cathodes of SOFCs. *Acta Mater.* **2008**, *56*, 4876–4889.

[20] Lu, C. L.; Niu, B. B.; Yi, W. D.; Ji, Y.; Xu, B. M. Efficient symmetrical electrodes of $PrBaFe_{2-x}Co_xO_{5+\delta}$ (x = 0, 0.2, 0.4) for solid oxide fuel cells and solid oxide electrolysis cells. *Electrochim. Acta* **2020**, *358*, 136916.

[21] Mao, X. B.; Yu, T.; Ma, G. L. Performance of cobalt-free double-perovskite $NdBaFe_{2-x}Mn_xO_{5+\delta}$ cathode materials for proton-conducting IT-SOFC. *J. Alloys Compd.* **2015**, *637*, 286–290.

[22] Chen, Y. H.; Cheng, Z. X.; Yang, Y.; Gu, Q. W.; Tian, D.; Lu, X. Y.; Yu, W. L.; Lin, B. Novel quasi-symmetric solid oxide fuel cells with enhanced electrochemical performance. *J. Power Sources* **2016**, *310*, 109–117.

[23] Zhang, B. Z.; Wan, Y. H.; Hua, Z. H.; Tang, K. B.; Xia, C. R. Tungsten-doped $PrBaFe_2O_{5+\delta}$ double perovskite as a high-performance electrode material for symmetrical solid oxide fuel cells. *ACS Appl. Energy Mater.* **2021**, *4*, 8401–8409.

[24] Li, G. D.; Gou, Y. J.; Cheng, X. J.; Bai, Z.; Ren, R. Z.; Xu, C. M.; Qiao, J. S.; Sun, W.; Wang, Z. H.; Sun, K. N. Enhanced electrochemical performance of the Fe-based layered perovskite oxygen electrode for reversible solid oxide cells. *ACS Appl. Mater. Interfaces* **2021**, *13*, 34282–34291.

[25] Zhang, B. Z.; Zhang, S. W.; Han, H. R.; Tang, K. B.; Xia, C. R. Cobalt-free double perovskite oxide as a promising cathode for solid oxide fuel cells. *ACS Appl. Mater. Interfaces* **2023**, *15*, 8253–8262.

[26] Shannon, R. D. Revised effective ionic radii and systematic studies of interatomic distances in halides and chalcogenides. *Acta Cryst. A* **1976**, *32*, 751–767.

[27] Ren, R. Z.; Wang, Z. H.; Meng, X. G.; Xu, C. M.; Qiao, J. S.; Sun, W.; Sun, K. N. Boosting the electrochemical performance of Fe-based layered double perovskite cathodes by Zn^{2+} doping for solid oxide fuel cells. *ACS Appl. Mater. Interfaces* **2020**, *12*, 23959–23967.

[28] Gao, J. T.; Liu, Y. Y.; Gao, Y.; Yuan, M. K.; Wang, Z.; Lü, Z.; Li, Q.; Wei, B. Cobalt-free fluorine doped $Bi_{0.7}Sr_{0.3}FeO_{3-\delta}$ oxides for energetic cathodes of low-temperature solid oxide fuel cells. *Chem. Eng. J.* **2023**, *452*, 139584.

[29] Jacobs, R.; Mayeshiba, T.; Booske, J.; Morgan, D. Material discovery and design principles for stable, high activity perovskite cathodes for solid oxide fuel cells. *Adv. Energy Mater.* **2018**, *8*, 1702708.

[30] Xi, X. A.; Liu, J. W.; Luo, W. Z.; Fan, Y.; Zhang, J. J.; Luo, J. L.; Fu, X. Z. Unraveling the enhanced kinetics of $Sr_2Fe_{1+x}Mo_{1-x}O_{6-\delta}$ electrocatalysts for high-performance solid oxide cells. *Adv. Energy Mater.* **2021**, *11*, 2102845.

[31] Fu, M.; Lin, X.; Tan, L. G.; Zhang, P.; Xie, H. J.; Tao, Z. T. Self-assembled Fe-doped $PrBaCo_2O_{5+\delta}$ composite cathodes with disorder transition region for intermediate-temperature solid oxide fuel cells. *Int. J. Hydrogen Energy* **2023**, *48*, 15229–15237.

[32] Zhuang, Z. C.; Li, Y. H.; Yu, R. H.; Xia, L. X.; Yang, J. R.; Lang, Z. Q.; Zhu, J. X.; Huang, J. Z.; Wang, J. O.; Wang, Y. et al. Reversely trapping atoms from a perovskite surface for high-performance and durable fuel cell cathodes. *Nat. Catal.* **2022**, *5*, 300–310.

[33] Niu, Y. H.; Zhou, Y. C.; Lv, W. Q.; Chen, Y.; Zhang, Y. X.; Zhang, W. L.; Luo, Z. Y.; Kane, N.; Ding, Y.; Soule, L. et al. Enhancing oxygen reduction activity and Cr tolerance of solid oxide fuel cell cathodes by a multiphase catalyst coating. *Adv. Funct. Mater.* **2021**, *31*, 2100034.

[34] Tan, T.; Wang, Z. M.; Qin, M. X.; Zhong, W. T.; Hu, J. H.; Yang, C. H.; Liu, M. L. *In situ* exsolution of core–shell structured $NiFe/FeO_x$ nanoparticles on $Pr_{0.4}Sr_{1.6}(NiFe)_{1.5}Mo_{0.5}O_{6-\delta}$ for CO_2 electrolysis. *Adv. Funct. Mater.* **2022**, *32*, 2202878.

[35] Xi, X. A.; Fan, Y.; Zhang, J. J.; Luo, J. L.; Fu, X. Z. *In situ* construction of hetero-structured perovskite composites with exsolved Fe and Cu metallic nanoparticles as efficient CO_2 reduction electrocatalysts for high performance solid oxide electrolysis cells. *J. Mater. Chem. A* **2022**, *10*, 2509–2518.

[36] Zhang, Y. X.; Chen, Y.; Li, M.; Yan, M. F.; Ni, M.; Xia, C. R. A high-precision approach to reconstruct distribution of relaxation times from electrochemical impedance spectroscopy. *J. Power Sources* **2016**, *308*, 1–6.

[37] Li, M.; Ren, Y. Y.; Zhu, Z. S.; Zhu, S. Y.; Chen, F. L.; Zhang, Y. X.; Xia, C. R. $La_{0.4}Bi_{0.4}Sr_{0.2}FeO_{3-\delta}$ as cobalt-free cathode for intermediate-temperature solid oxide fuel cell. *Electrochim. Acta* **2016**, *191*, 651–660.

[38] Du, Z. W.; He, F.; Gao, H.; Xu, Y. S.; Zhu, F.; Xu, K.; Xia, J. J.; Zhang, H.; Huang, Y. X.; Liu, Y. et al. An active bifunctional Pd-doped double perovskite air electrode for reversible protonic ceramic electrochemical cells. *Energy Storage Mater.* **2024**, *68*, 103345.

[39] Ma, Y. M.; Zhang, L. J.; Zhu, K.; Zhang, B. Z.; Peng, R. R.; Xia, C. R.; Huang, L. In^{3+}-doped $Sr_2Fe_{1.5}Mo_{0.5}O_{6-\delta}$ cathode with improved performance for an intermediate-temperature solid oxide fuel cell. *Nano Res.* **2023**, *17*, 407–415.

[40] Hu, T.; Zhu, F.; Xia, J. J.; He, F.; Du, Z. W.; Zhou, Y. C.; Liu, Y.; Wang, H. B.; Chen, Y. *In situ* engineering of a cobalt-free perovskite air electrode enabling efficient reversible oxygen reduction/evolution reactions. *Adv. Funct. Mater.* **2023**, *33*, 2305567.

[41] Xu, Z. Q.; Hu, X. Y.; Wan, Y. H.; Xue, S. S.; Zhang, S. W.; Zhang, L. J.; Zhang, B. Z.; Xia, C. R. Electrochemical performance and anode reaction process for Ca doped $Sr_2Fe_{1.5}Mo_{0.5}O_{6-\delta}$ as electrodes for symmetrical solid oxide fuel cells. *Electrochim. Acta.* **2020**, *341*, 136067.

[42] Zhu, T. L.; Troiani, H. E.; Mogni, L. V.; Han, M. F.; Barnett, S. A. Ni-substituted Sr(Ti, Fe)O_3 SOFC anodes: Achieving high performance via metal alloy nanoparticle exsolution. *Joule* **2018**, *2*, 478–496.

[43] Chen, M.; Chen, D. C.; Chang, M. L.; Hu, H. W.; Xu, Q. New insight into hydrogen oxidation reaction on $La_{0.3}Sr_{0.7}Fe_{0.7}Cr_{0.3}O_{3-\delta}$ perovskite as a solid oxide fuel cell anode. *J. Electrochem. Soc.* **2017**, *164*, F405–F411.